Supporting information for: Artefact suppression in 5-pulse Double Electron Electron Resonance for distance distribution measurements

Frauke D. Breitgoff, Janne Soetbeer, Andrin Doll, Gunnar Jeschke, and Yevhen O. Polyhach*

1 Pulse sequences and observer subsequence decays

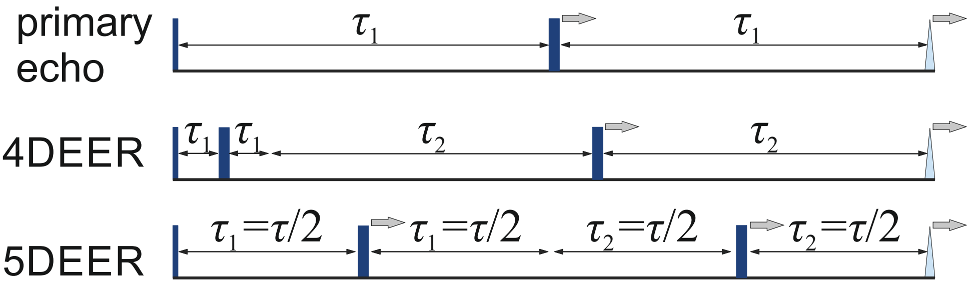

Fig. S1: Schematic representation of pulse sequences for echo decay measurements.

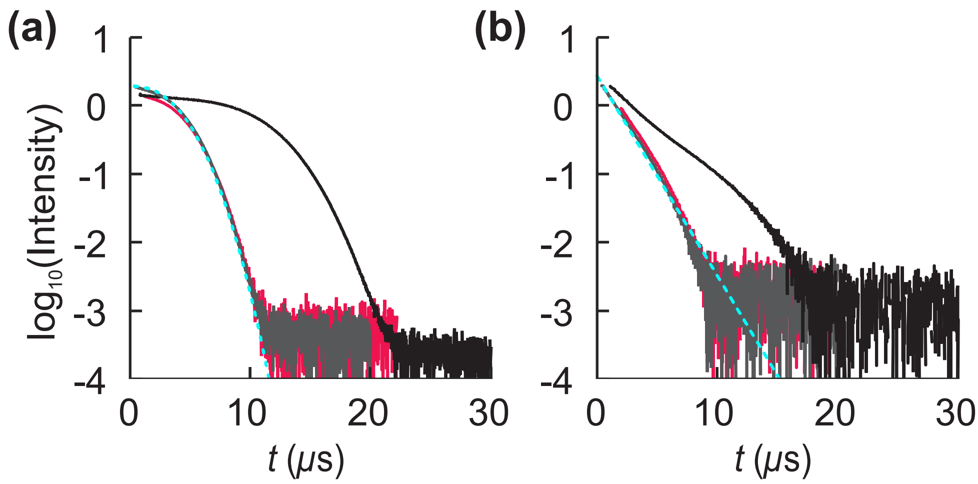

Fig. S2: Decay traces (log scale) of Hahn echo (grey), 4-pulse (red) and 5-pulse DEER (black) observer subsequences obtained at Q band at a temperature of 50 K. Dashed cyan lines are fits to the Hahn echo decay. (a) 40 μM TEMPOL in H_2O/glycerol (no deuteration). Stretched exponential fit to the Hahn echo decay with ($\kappa \approx 2.4$) and $T_m \approx 4.6$ μs. (b) 20 μM singly labeled WALP23 (W3R1) in DOPC bilayer/H_2O. Monoexponential fit to the Hahn echo decay with $T_m \approx 1.8$ μs (red dashed line).

2 Various pump pulses in symmetric 4-DEER

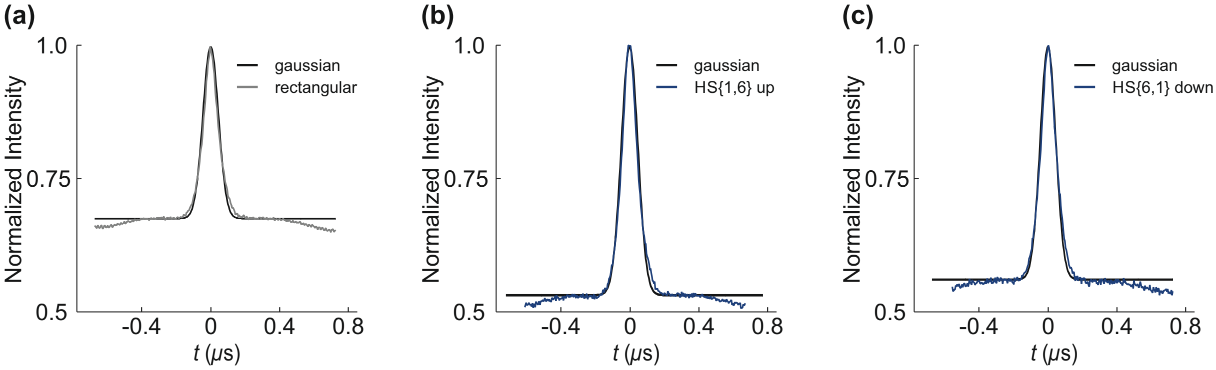

Fig. S3: 4-pulse DEER measurements with symmetric (Carr-Purcell) timings of WALP23 (A7R1,W22R1). The respective pump pulse was a monochromatic pulse of 12 ns length **(a)** or 200 ns HS16 pulse with increasing **(b)** or decreasing **(c)** frequency. For comparison of the (a)symmetry in the DEER signal, a Gaussian is overlaid. No considerable difference in asymmetry of the DEER signal measured with HS16 pump pulse with respect to the DEER signal measured with the rectangular monochromatic pump pulse is observed.

3 Comparison of Phase Cycling and Application of shift in 5-pulse DEER

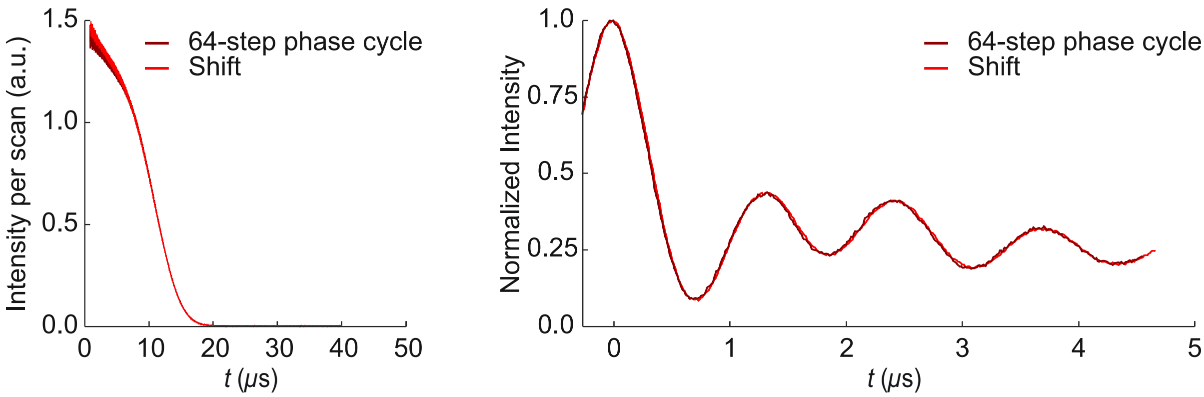

Fig. S4: Relaxation and 5-pulse DEER measurements with 64-step phase cycle [1] are compared to measurements with a time shift δ of the last pulse. Relaxation traces measured for TEMPOL in H_2O/glycerol for 5-pulse DEER observer subsequence (left). 5-pulse DEER traces of the rigid biradical MSA236 in deuterated *ortho*-terphenyl (right). Dark red: measurement with 64-step phase cycle and no shift; Light red: measurement with shift δ and 8-step phase cycle, i.e. [+(+x)-(-x)] on the $\pi/2$ pulse and [+(+x)-(+y)+(-x)-(-y)] on the moving pump pulse. The measurements with time shift and 8-step phase cycle show no deviation from the measurements with the full phase cycle. Measurements were performed at Q band, 50 K.

4 Nuclear Modulation Averaging

Implementing nuclear modulation averaging analogously to the way it is implemented in 4-pulse DEER leads to broadening of the partial excitation artefact (Fig. S5a,b). The dynamical decoupling condition is preserved by incrementing all observer subsequence delays simultaneously. Hereby, the delay $(\tau + \delta)$ before the last observer π-pulse is incremented by twice the nuclear modulation averaging increment and the delay $(\tau/2 + \delta)$ before the detection event is incremented by once the nuclear modulation averaging increment (Fig. S5a). Consequently, the artefact gets stepwise shifted to later time, while the main 5-pulse DEER signal remains at the same time t'. If the partial excitation artefact is not completely suppressed experimentally and has to be removed in data processing, such broadening of the partial excitation artefact leads to erroneous correction.

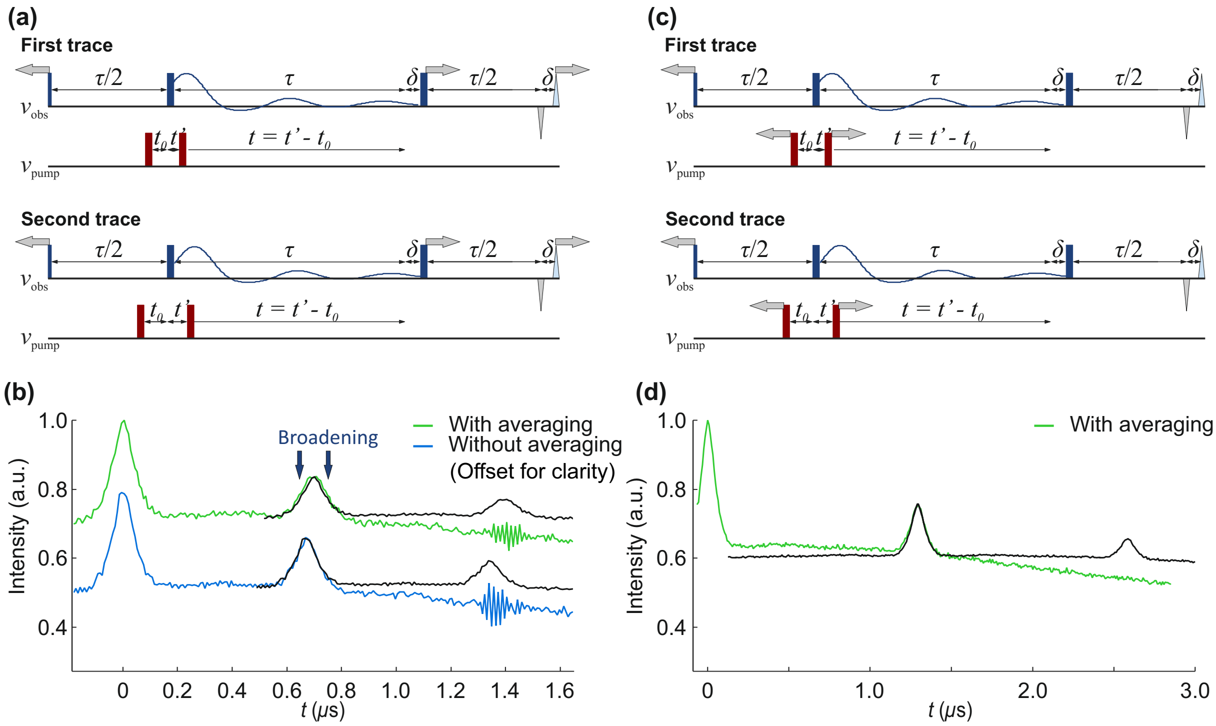

Fig. S5: Two possible implementations of nuclear modulation averaging in 5-pulse DEER (shifting of pulses indicated by horizontal arrows) and corresponding DEER traces from WALP23 (A7R1, W22R1) at Q band, 50 K (averaging $8 \cdot 16$ ns). For comparison, 5-pulse DEER traces are also shown shifted and scaled to the partial excitation artefact (black). **(a)** Pulse sequence preserving the dynamical decoupling condition of the observer subsequence. **(b)** 5-pulse DEER traces measured with and without nuclear modulation averaging corresponding to the pulse sequence shown in **(a)**. Pump pulses were rectangular (12 ns). **(c)** Pulse sequence avoiding broadening of the partial excitation artefact. **(d)** 5-pulse DEER traces measured with nuclear modulation averaging corresponding to the pulse sequence shown in **(b)**. Pump pulses were HS{1,6}, 100 ns long, 150 MHz wide, offset 70 MHz from ν_{obs}.

To circumvent broadening of the artefact, we kept the delay between the $\pi/2$-pulse and the standing pump pulse constant (Fig. S5c). To counteract the resulting shift of the main 5-pulse signal with t_0, we simultaneously increment the initial delay t' before the moving pump pulse. In this implemention of nuclear modulation averaging, the dynamical decoupling condition is not strictly preserved. However, as the change in delays by nuclear averaging is usually small in relation to τ, the loss in signal intensity is expected to be minor. Broadening of the partial excitation artefact was successfully suppressed with this implementation of nuclear modulation averaging (Fig. S5c,d).

Note, however, that for most of our measurements, no nuclear modulation averaging was necessary. Application of nuclear modulation averaging in 5-pulse DEER therefore still remains to be rigorously studied.

5 Distance distributions extracted from 4- and 5-pulse DEER data

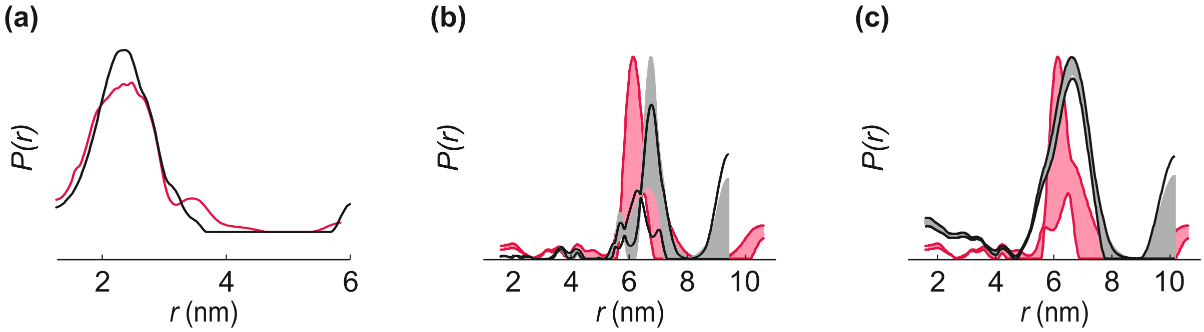

Fig. S6: Distance distributions $P(r)$ from 4-pulse (red) and 5-pulse DEER (black). (a) P(r) from X-band data from WALP mutant A7R1/W22R1 shown in Fig. 6 of the main paper. (b) Uncertainty estimates for $P(r)$ from 5-pulse DEER measured with $\tau = 8$ μs and 4-pulse DEER acquired with $\tau = 5$ μs for an HDL particle (Fig. 8(a) of main paper). (c) Uncertainty estimates for $P(r)$ from 5-pulse DEER measured for $\tau = 10$ μs and 4-pulse DEER acquired with $\tau = 5$ μs for an HDL particle (Fig. 8(b) of main paper). Uncertainty estimates were computed with the Validation tool (DeerAnalysis).[2]

6 Product Operator Calculations

The pulse sequence was described by a series of pulses and free evolution under the Hamiltonian $\hat{\mathcal{H}}_0$.

$$\hat{\mathcal{H}}_0 = \omega_{dd}\hat{S}_{o,z}\hat{S}_{p,z} \tag{1}$$

Pulses are denoted as $\beta_{\hat{S}_k}$ with flip angle β acting on spin k (k = o observer, k = p pumped spin). i.e. $\pi_{\hat{S}_p}$ is a π pulse acting on the pumped spin. Free evolution under the Hamiltonian $\hat{\mathcal{H}}_0$ for the time t is denoted by $\hat{\mathcal{H}}_0(t)$. For the "ideal" 5-pulse pathway, the following sequence results:

$$\begin{aligned}
&\sigma_{\text{eq}} \xrightarrow{\pi/2_{\hat{S}_o}} \sigma_1 \xrightarrow{\hat{\mathcal{H}}_0(\tau/2-t_0)} \sigma_2 \xrightarrow{\pi_{\hat{S}_p}} \sigma_3 \xrightarrow{\hat{\mathcal{H}}_0(t_0)} \sigma_4 \xrightarrow{\pi_{\hat{S}_o}} \sigma_5 \\
&\xrightarrow{\hat{\mathcal{H}}_0(t')} \sigma_6 \xrightarrow{\pi_{\hat{S}_p}} \sigma_7 \xrightarrow{\hat{\mathcal{H}}_0(\tau-t'+\delta)} \sigma_8 \xrightarrow{\pi_{\hat{S}_o}} \sigma_9 \xrightarrow{\hat{\mathcal{H}}_0(\tau/2+\delta)} \sigma_{10}
\end{aligned} \tag{2}$$

With the full expressions for σ, for the "ideal" 5-pulse DEER pathway one obtains

$$\begin{aligned}
\sigma_{eq} &= -I_z - S_z \\
&\xrightarrow{\pi/2_{\hat{S}_o}} I_y - S_z \\
&\xrightarrow{\hat{\mathcal{H}}_0(\tau/2-t_0)} \cos\left[d\left(t_0 - \frac{\tau}{2}\right)\right] I_y - S_z + 2S_zI_x \sin\left[d\left(t_0 - \frac{\tau}{2}\right)\right] \\
&\xrightarrow{\pi_{\hat{S}_p}} \cos\left[d\left(t_0 - \frac{\tau}{2}\right)\right] I_y + S_z - 2S_zI_x \sin\left[d\left(t_0 - \frac{\tau}{2}\right)\right] \\
&\xrightarrow{\hat{\mathcal{H}}_0(t_0)} \cos\left[d\left(2t_0 - \frac{\tau}{2}\right)\right] I_y + S_z - 2S_zI_x \sin\left[d\left(2t_0 - \frac{\tau}{2}\right)\right] \\
&\xrightarrow{\pi_{\hat{S}_o}} -\cos\left[d\left(2t_0 - \frac{\tau}{2}\right)\right] I_y + S_z - 2S_zI_x \sin\left[d\left(2t_0 - \frac{\tau}{2}\right)\right] \\
&\xrightarrow{\hat{\mathcal{H}}_0(t')} -\cos\left[d\left(2t_0 - \frac{\tau}{2} - t'\right)\right] I_y + S_z - 2S_zI_x \sin\left[d\left(2t_0 - \frac{\tau}{2} - t'\right)\right] \\
&\xrightarrow{\pi_{\hat{S}_p}} -\cos\left[d\left(2t_0 - \frac{\tau}{2} - t'\right)\right] I_y - S_z + 2S_zI_x \sin\left[d\left(2t_0 - \frac{\tau}{2} - t'\right)\right] \\
&\xrightarrow{\hat{\mathcal{H}}_0(\tau-t'+\delta)} -\cos\left[d\left(2t_0 + \delta + \frac{\tau}{2} - 2t'\right)\right] I_y - S_z + 2S_zI_x \sin\left[d\left(2t_0 + \delta + \frac{\tau}{2} - 2t'\right)\right] \\
&\xrightarrow{\pi_{\hat{S}_o}} \cos\left[d\left(2t_0 + \delta + \frac{\tau}{2} - 2t'\right)\right] I_y - S_z + 2S_zI_x \sin\left[d\left(2t_0 + \delta + \frac{\tau}{2} - 2t'\right)\right] \\
&\xrightarrow{\hat{\mathcal{H}}_0(\tau/2+\delta)} \cos\left[2d\left(t_0 - t'\right)\right] I_y - S_z + 2S_zI_x \sin\left[2d\left(t_0 - t'\right)\right].
\end{aligned} \tag{3}$$

The expression for the coherence transfer pathway 2 in table 1 in the main paper (first band overlap artefact) is obtained as follows:

$$
\begin{aligned}
\sigma_{eq} &= -I_z - S_z \qquad (4)\\
&\xrightarrow{\pi/2\hat{S}_o} I_y - S_z\\
&\xrightarrow{\hat{\mathcal{H}}_0(\tau/2-t_0)} \cos\left[d\left(t_0-\frac{\tau}{2}\right)\right] I_y - S_z + 2S_zI_x \sin\left[d\left(t_0-\frac{\tau}{2}\right)\right]\\
&\xrightarrow{\pi\hat{S}_p} \cos\left[d\left(t_0-\frac{\tau}{2}\right)\right] I_y + S_z - 2S_zI_x \sin\left[d\left(t_0-\frac{\tau}{2}\right)\right]\\
&\xrightarrow{\hat{\mathcal{H}}_0(t_0)} \cos\left[d\left(2t_0-\frac{\tau}{2}\right)\right] I_y + S_z - 2S_zI_x \sin\left[d\left(2t_0-\frac{\tau}{2}\right)\right]\\
&\xrightarrow{\pi\hat{S}_o} -\cos\left[d\left(2t_0-\frac{\tau}{2}\right)\right] I_y + S_z - 2S_zI_x \sin\left[d\left(2t_0-\frac{\tau}{2}\right)\right]\\
&\xrightarrow{\pi\hat{S}_p} -\cos\left[d\left(2t_0-\frac{\tau}{2}\right)\right] I_y - S_z + 2S_zI_x \sin\left[2dt_0-\left(\frac{d\tau}{2}\right)\right]\\
&\xrightarrow{\hat{\mathcal{H}}_0(t')} -\cos\left[d\left(2t_0-\frac{\tau}{2}-t'\right)\right] I_y - S_z + 2S_zI_x \sin\left[d\left(2t_0-\frac{\tau}{2}+t'\right)\right]\\
&\xrightarrow{\pi\hat{S}_p} -\cos\left[d\left(2t_0-\frac{\tau}{2}+t'\right)\right] I_y + S_z - 2S_zI_x \sin\left[d\left(2t_0-\frac{\tau}{2}+t'\right)\right]\\
&\xrightarrow{\hat{\mathcal{H}}_0(\tau-t'+\delta)} -\cos\left[d\left(-2t_0+\delta+\frac{3\tau}{2}-2t'\right)\right] I_y + S_z + 2S_zI_x \sin\left[d\left(-2t_0+\delta+\frac{3\tau}{2}-2t'\right)\right]\\
&\xrightarrow{\pi\hat{S}_o} \cos\left[d\left(-2t_0+\delta+\frac{3\tau}{2}-2t'\right)\right] I_y + S_z + 2S_zI_x \sin\left[d\left(-2t_0+\delta+\frac{3\tau}{2}-2t'\right)\right]\\
&\xrightarrow{\hat{\mathcal{H}}_0(\tau/2+\delta)} \cos\left[2d\left(t_0-\frac{\tau}{2}+2t'\right)\right] I_y + S_z - 2S_zI_x \sin\left[2d\left(t_0-\frac{\tau}{2}+t'\right)\right].
\end{aligned}
$$

The expression for coherence transfer pathway 3 (second band overlap artefact) results from:

$$
\begin{aligned}
\sigma_{eq} &= -I_z - S_z \qquad (5)\\
&\xrightarrow{\pi/2_{\hat{S}_o}} I_y - S_z\\
&\xrightarrow{\hat{\mathcal{H}}_0(\tau/2-t_0)} \cos\left[d\left(t_0-\frac{\tau}{2}\right)\right] I_y - S_z + 2S_zI_x\sin\left[d\left(t_0-\frac{\tau}{2}\right)\right]\\
&\xrightarrow{\pi_{\hat{S}_p}} \cos\left[d\left(t_0-\frac{\tau}{2}\right)\right] I_y + S_z - 2S_zI_x\sin\left[d\left(t_0-\frac{\tau}{2}\right)\right]\\
&\xrightarrow{\hat{\mathcal{H}}_0(t_0)} \cos\left[d\left(2t_0-\frac{\tau}{2}\right)\right] I_y + S_z - 2S_zI_x\sin\left[d\left(2t_0-\frac{\tau}{2}\right)\right]\\
&\xrightarrow{\pi_{\hat{S}_o}} -\cos\left[d\left(2t_0-\frac{\tau}{2}\right)\right] I_y + S_z - 2S_zI_x\sin\left[d\left(2t_0-\frac{\tau}{2}\right)\right]\\
&\xrightarrow{\hat{\mathcal{H}}_0(t')} -\cos\left[d\left(2t_0-\frac{\tau}{2}-t'\right)\right] I_y + S_z - 2S_zI_x\sin\left[d\left(2t_0-\frac{\tau}{2}-t'\right)\right]\\
&\xrightarrow{\pi_{\hat{S}_p}} -\cos\left[d\left(2t_0-\frac{\tau}{2}-t'\right)\right] I_y - S_z + 2S_zI_x\sin\left[d\left(2t_0-\frac{\tau}{2}-t'\right)\right]\\
&\xrightarrow{\hat{\mathcal{H}}_0(\tau-t'+\delta)} -\cos\left[d\left(2t_0+\delta+\frac{\tau}{2}-2t'\right)\right] I_y - S_z + 2S_zI_x\sin\left[d\left(2t_0+\delta+\frac{\tau}{2}-2t'\right)\right]\\
&\xrightarrow{\pi_{\hat{S}_o}} -\cos\left[d\left(2t_0+\delta+\frac{\tau}{2}-2t'\right)\right] I_y - S_z + 2S_zI_x\sin\left[d\left(2t_0+\delta+\frac{\tau}{2}-2t'\right)\right]\\
&\xrightarrow{\pi_{\hat{S}_p}} \cos\left[d\left(2t_0+\delta+\frac{\tau}{2}-2t'\right)\right] I_y + S_z - 2S_zI_x\sin\left[d\left(2t_0+\delta+\frac{\tau}{2}-2t'\right)\right]\\
&\xrightarrow{\hat{\mathcal{H}}_0(\tau/2+\delta)} \cos\left[2d\left(t_0+\frac{\tau}{2}+\delta-t'\right)\right] I_y + S_z - 2S_zI_x\sin\left[2d\left(t_0+\frac{\tau}{2}+\delta-t'\right)\right].
\end{aligned}
$$

Detected are only terms which correspond to transverse magnetization, i.e. I_x and I_y. Accordingly, the argument of the cosine modulation of I_y of the final density operator is used to obtain the zero time of the individual contributions in Table 1 of the main paper.

7 Crossing echoes on incoherent spectrometers

Experimental 5-pulse DEER traces recorded on the incoherent spectrometer (Bruker Elexsys E680) contained a distortion at late dipolar evolution times (Fig. 7 in the main text). According to Tait and Stoll [1], there are several echoes that cross the wanted DEER echo within the last quarter of the 5-pulse DEER trace. We observed that the echoes cross at a time t' that varies linearly with t_0 (see Fig. S5 for delay nomenclature). According to the notation in the paper by Tait and Stoll, this corresponds to a change in $t_{\mathrm{DEER,cross}}$ with $2t_2$ (where t_2 is the delay between the static pump pulse and the first refocusing observer pulse) due to a different definition of the time axis. This observation eliminates all but three coherence transfer pathways satisfying these requirements. They are summarized in Table S1 (nomenclature of echoes according to Tait and Stoll).[1] Among those echoes, $\mathrm{PE}_{1\mathrm{p}'\mathrm{p}}$ and $\mathrm{dPE}_{[1\mathrm{p}'\mathrm{p}]3}$ share the property that neither the π observer pulse in between the two pump pulses nor the two pump pulses taken together change the observer spin coherence order. The signal due to such coherence transfer pathways is not expected to average even if the pump pulses are incoherent.

Table S1: Echoes in forward 5-DEER with $\frac{3}{4}\tau \leq t' \leq \tau$ according to Tait and Stoll [1] that shift linearly with t_0. Coherence order change by the individual pulses is indicated.

Echo	obs. coh. order	t'	$\pi/2$	$\mathrm{pump}_{\mathrm{stat}}$	π_{obs} 1	$\mathrm{pump}_{\mathrm{var}}$	π_{obs} 2
$\mathrm{PE}_{1\mathrm{p}'\mathrm{p}}$	- + + - -	$\tau+\delta-t_0$	-1	2	0	-2	0
$\mathrm{dPE}_{[1\mathrm{p}'\mathrm{p}]3}$	+ 0 0 + -	$\tau-t_0$	1	-1	0	1	-2
$\mathrm{SE}_{(\mathrm{SE}1\mathrm{p}'2)\mathrm{p}3}$	- 0 + 0 -	$\tau+\delta-t_0$	-1	1	1	-1	-1

Experiments on the commercial spectrometer featuring incoherent pump-observer excitation with phase-locked pump pulses (within one individual scan) and using only the pulses needed to generate the corresponding coherence transfer pathway revealed that both $\mathrm{PE}_{1\mathrm{p}'\mathrm{p}}$ and $\mathrm{dPE}_{[1\mathrm{p}'\mathrm{p}]3}$ contribute to the echo crossing artefact in question. The former, stemming from an electron coherence excited by the first $\pi/2$ observer pulse and refocused by two pump pulses, makes a smaller contribution. The latter ($\mathrm{dPE}_{[1\mathrm{p}'\mathrm{p}]3}$ pathway), is a virtual echo formed by the same pulses as in $\mathrm{PE}_{1\mathrm{p}'\mathrm{p}}$ that is refocused by the second observer π pulse. This echo made the strongest contribution to the echo crossing artefact in the 5-pulse DEER trace because for a long time interval magnetization is stored along z where it decays with the longitudinal relaxation time. In contrast, for the echo associated with the $\mathrm{PE}_{1\mathrm{p}'\mathrm{p}}$ pathway coherence always decays with the transverse relaxation time.

Separation of the individual crossing echo contributions was performed by phase cycling [3] on the home-built coherent spectrometer (Fig. S7). When the phase of both pump pulses was stepped together selecting a coherence order change 0 by a 4-step phase cycle [+(+x)+(+y)+(-x)+(-y)], all crossing echoes vanish except for two contributions with timings $\tau + \delta - t_0$ and $\tau - t_0$ (green trace). This corresponds to the situation encountered with a spectrometer with incoherent pump pulse channel (Fig 7 main text). Selecting coherence order change 2 by the last observer π pulse by a [+(+x)-(+y)+(-x)-(-y)] phase cycle on this pulse eliminates the echo $PE_{1p'p}$ because this echo features a coherence order change of 0 for this pulse (purple trace). If instead of the second observer π pulse the first observer π pulse is phase cycled, again selecting coherence order change 2 by a 4 step [+(+x)-(+y)+(-x)-(-y)] phase cycle, both $PE_{1p'p}$ and $dPE_{[1p'p]3}$ crossing echo contributions are eliminated due to their coherence order change $\neq 2$ (yellow trace). The 5-pulse DEER trace acquired with this phase cycle shows no deviation from the trace recorded with a 128 step phase cycle varying the phases of all pulses (blue) or the trace recorded phase cycling all three observer pulses (orange in Fig. S7).

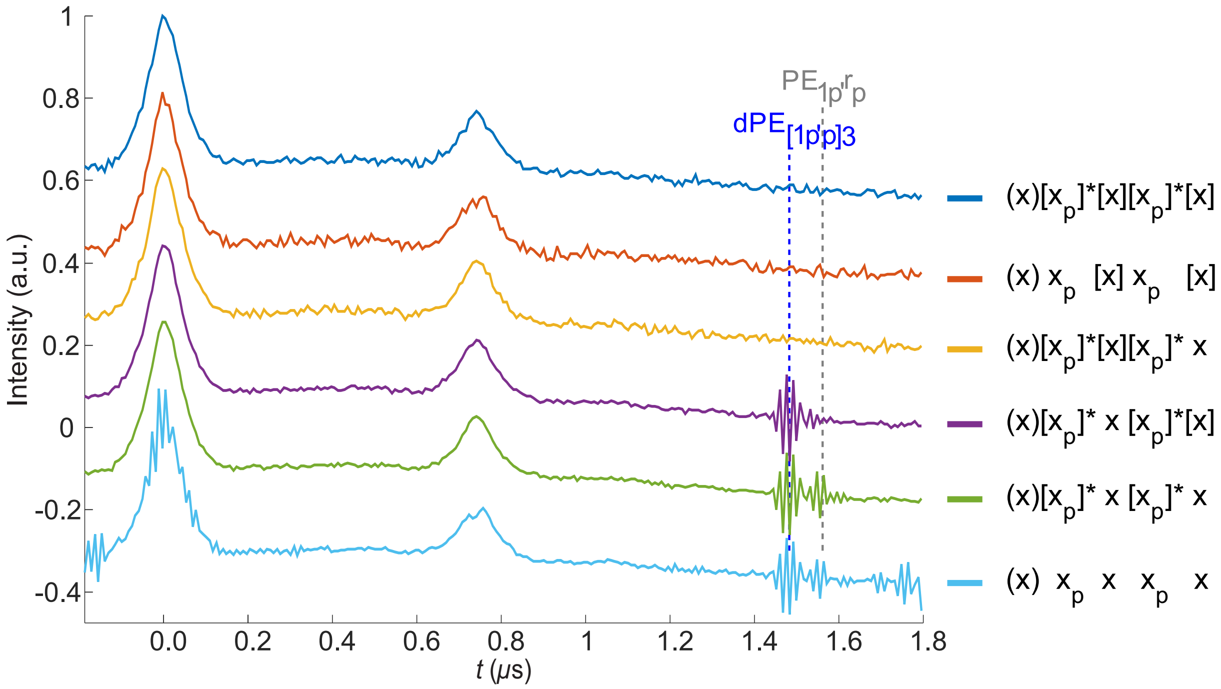

Fig. S7: Phase cycling in 5-pulse DEER. DEER traces were recorded with 32 ns observer pulses and rectangular 12 ns pump pulses, offset from the observer frequency by 100 MHz. Phase cycling is indicated as ( ) for 2-step and [ ] for 4-step, where the asterisk denotes that the two pump pulses were phase cycled simultaneously to mimic measurement conditions of a spectrometer with incoherent pump pulse channel. Traces offset for clarity.

8 Implementation of HSh and HS$\{h_1,h_2\}$ pulses

The selectivity of the HS pulse is a direct consequence of offset-independent adiabaticity [4]: The modulation functions formally establish offset-independent adiabaticity for all excited spins, even for those at the edges of the pulse. In this sense, the HS1 pulse allows for an *adiabatic edge truncation* provided that β is large enough. The adiabaticity factor of the HS1 pulse [5] can be rewritten as

$$Q_{\mathrm{crit}}^{\mathrm{HS1}} = \frac{4\pi \cdot \nu_{1,\mathrm{max}}^2 \cdot t_\mathrm{p}}{\beta \cdot \Delta f} = \frac{2}{\beta} \cdot Q_{\mathrm{crit}}^{\mathrm{lin}} \tag{6}$$

where $Q_{\mathrm{crit}}^{\mathrm{lin}}$ is the expression for constant-rate chirps. As compared to a constant-rate chirp, the selective inversion profile of the HS1 pulse ($\beta \approx 10$) therefore degrades the adiabaticity by a factor of 5.

Since HS1 pulses for selective inversion ($\beta \approx 10$) have such a pronounced trade-off in adiabaticity [5], HS pulses of higher orders have been introduced [4], which are referred to as HSh pulses. The modulation functions for these pulses are given in the main text.

For $h = 1$, the solution to the integral in Eq. (5) in the main text is given in Eq. (6) in the main text. For $h > 1$, the integral needs to be solved numerically. Accordingly, also the adiabaticity Q_{crit} needs to be computed numerically. Note that a variety of definitions of the parameters β, h and the time axis $\tilde{t} = t/t_\mathrm{p}$ for HS1 and HSh pulses is used in the literature. With our choice and the normalization of the integral in Eq. (5) in the main text, the sweep width Δf is independent on both h and β.

The influence of h on selectivity is shown in Fig. S8. Panels (a) and (b) illustrate the amplitude and frequency modulation functions, respectively, in ascending order n from 1 to 8. The arrows denote the changes along ascending h. In order to have the same adiabaticity Q_{crit} for all orders h, the pulse lengths were chosen as t_p = [400, 188, 143, 124, 114, 108, 103, 100] ns. The parametrization of the selectivity of pulses with order h becomes apparent in the simulations of $\left\langle \hat{S}_z \right\rangle$ for $Q_{\mathrm{crit}} = 5$ and $Q_{\mathrm{crit}} = 2 \cdot \log(2)/\pi$ in panels (c) and (d), respectively.

The spectral distribution of the spin packets to be excited may not require frequency selectivity on both sides of the excitation window. One can therefore combine HSh pulses of different orders. Such combined HSh pulses are referred to as HS$\{h_1, h_2\}$ pulses, where h_1 is the order of the first half of the combined pulse and h_2 is the order of the second half. If $h_1 \neq h_2$, we refer to an asymmetric HS pulse.

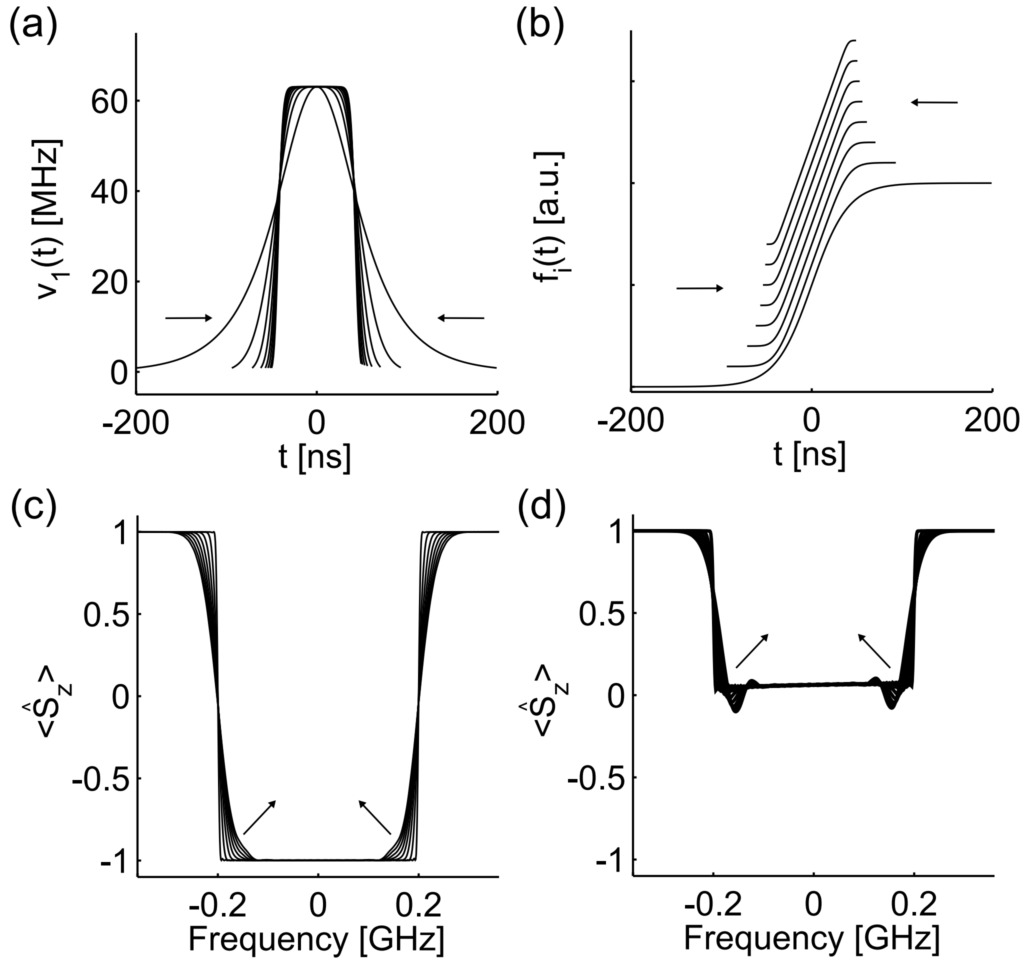

Fig. S8: Selectivity parametrization of HSh pulses with $\Delta f = 400$ MHz, $\beta = 10$, identical peak amplitude and identical adiabaticity Q_{crit}. The illustrated curves correspond to ascending orders h from 1 to 8. The consequences of increasing h are illustrated by means of arrows. (a) Amplitude modulation functions $\nu_1(t)$. (b) Frequency modulation functions $f_{\mathrm{i}}(t)$, vertically displaced. (c) Simulation of $\left\langle \hat{S}_z \right\rangle$ for $Q_{\mathrm{crit}} = 5$. (d) Simulation of $\left\langle \hat{S}_z \right\rangle$ for $Q_{\mathrm{crit}} = 2 \cdot \log(2)/\pi$, which corresponds to a peak amplitude of $\nu_1 = 18.74$ MHz. All simulations performed with SPIDYAN.[6]

The superior frequency selectivity of HSh and HS$\{h_1, h_2\}$ pulses thanks to their *adiabatic edge truncation* is interesting for a number of applications in EPR spectroscopy. However, these pulses only fulfill offset-independent adiabaticity in the absence of any bandwidth limitations imposed by the resonator. The incorporation of a resonator profile $\nu_1(f)$ into HS pulses is performed in an analogous manner to the compensation of constant-rate chirps introduced previously.[7] As a result, the procedure generates a HS$\{h_1, h_2\}$ pulse with its time axis *warped* for offset-independent adiabaticity in presence of the bandwidth limitation $\nu_1(f)$.[8]

References

(1) C. E. Tait and S. Stoll, *Phys. Chem. Chem. Phys.*, 2016, **18**, 18470–18485.

(2) G. Jeschke, V. Chechik, P. Ionita, A. Godt, H. Zimmermann, J. Banham, C. R. Timmel, D. Hilger and H. Jung, *Appl. Magn. Reson.*, 2006, **30**, 473–498.

(3) C. Gemperle, G. Aebli, A. Schweiger and R. Ernst, *J. Magn. Reson.*, 1990, **88**, 241–256.

(4) A. Tannus and M. Garwood, *J. Magn. Reson. A*, 1996, **120**, 133–137.

(5) E. Kupce and R. Freeman, *J. Magn. Reson. A*, 1995, **117**, 246–256.

(6) S. Pribitzer, A. Doll and G. Jeschke, *J. Magn. Reson.*, 2016, **263**, 45–54.

(7) A. Doll, S. Pribitzer, R. Tschaggelar and G. Jeschke, *J. Magn. Reson.*, 2013, **230**, 27–39.

(8) A. Doll, Ph.D. Thesis, ETH Zurich, 2016.